J|A|C|S ARTICLES

Published on Web 02/15/2010

Versatile Phosphate Phosphors $ABPO_4$ in White Light-Emitting Diodes: Collocated Characteristic Analysis and Theoretical Calculations

Chun Che Lin,[†] Zhi Ren Xiao,[‡] Guang-Yu Guo,[§,‡] Ting-Shan Chan,[⊥] and Ru-Shi Liu*,[†]

Department of Chemistry and Department of Physics, National Taiwan University, Taipei 106, Taiwan, Graduate Institute of Applied Physics, National Chengchi University, Taipei 116, Taiwan, and National Synchrotron Radiation Research Center, Hsinchu 300, Taiwan

Received October 30, 2009; E-mail: rsliu@ntu.edu.tw

Abstract: The orthophosphate host family, $A^IB^{II}PO_4$ (A^I = monovalent cation, B^{II} = divalent cation), has recently been made available as phosphors that combine with near-UV lighting chips for use in solid-state white light-emitting diodes (LEDs). This study elucidates the crystalline structure and lattice parameters of the products via a solid-state reaction, using powder X-ray diffraction (XRD) and GSAS refinement. The versatility of the phosphor host $A^IB^{II}PO_4$ is established by examining isovalent substitutions of four cations in the structure—Li or K for A^I, Sr or Ba for B^{II}—and three doped activators, RE = Eu^{2+}, Tb^{3+}, and Sm^{3+}. The luminescence properties, decay time, and Commission Internationale de l'Éclairage (CIE) chromaticity index are determined for various concentrations of these activators and metal constituents of the host. The thermal stabilities of all of these compounds are determined for the first time from the crystal structure and the coordination environment of the rare-earth metal. The morphology, composition, and particle size were measured in detail. Finally, density functional calculations were performed using the generalized gradient approximation plus an on-site Coulombic interaction correction (GGA+U) scheme to investigate the electronic structures of the $KSrPO_4$ system. A concise model was proposed to explain the luminescence mechanism.

Introduction

InGaN-based white light-emitting diodes, which are regarded as the next-generation light source, have attracted substantial attention for use in display lighting sources and illuminating systems because of their high energy efficiency, durability, reliability, products of various sizes, and ecofriendly constituents.[1] A recent surge of research on LEDs has given us new opportunities and challenges. Generally, white light can be obtained from LEDs by three methods. The first pertains to the blue-excitation LED, in which the yellow-emitting YAG:Ce^{3+} phosphor is excited by an InGaN chip and possesses poor color-rendering index at long wavelengths.[2] The second strategy involves a complicated circuit, in which red, green, and blue components of LED chips are mixed, yielding a white LED. The third procedure is to use the combination of ultraviolet (UV) or blue emission LED chips and the red/green/yellow/blue light emitted from the phosphors; this latter white LED provides superior color uniformity with a high color rendering index (Ra) and excellent quality of light.[3] Among numerous phosphor candidates, such as $(Y,Tb)_3Al_5O_{12}:Ce^{3+}$, $(Sr,Ba)_2SiO_4:Eu^{2+}$, $(Sr,Ca)AlSiN_3:Eu^{2+}$, and $Sr_2Si_5N_8:Eu^{2+}$, have been commercialized and employed in white LED lamps for display and illumination.[2,4] This present work focuses on the development of an appropriate host and its chemical and physical effects formed by activators on characteristic properties for application in white LEDs.

The 1990s saw a wealth of research into the characteristics of crystal solution phases $ALiPO_4$ (A = Sr, Ba, and Pb), that is about their structures which have been elucidated by vis/UV spectroscopy, SHG measurements, ^{31}P magic angle spinning (MAS) NMR, and Raman spectroscopy. However, phosphor $LiSrPO_4:Eu^{2+}$ exhibits a strong broad absorption at 400 nm associated with the 5d−4f transition in various lattices. It

[†] Department of Chemistry, National Taiwan University.
[‡] Department of Physics, National Taiwan University.
[§] Graduate Institute of Applied Physics, National Chengchi University.
[⊥] National Synchrotron Radiation Research Center.

(1) (a) Nakamura, S.; Mukai, T.; Senoh, M. *Appl. Phys. Lett.* **1994**, *64*, 1687. (b) Nishida, T.; Ban, T.; Kobayashi, N. *Appl. Phys. Lett.* **2003**, *82*, 3817. (c) Schubert, E. F.; Kim, J. K. *Science* **2005**, *308*, 1274. (d) Hashimoto, T.; Wu, F.; Speck, J. S.; Nakamura, S. *Nat. Mater.* **2007**, *6*, 568.

(2) (a) Xie, R.-J.; Hirosaki, N.; Sakuma, K.; Yamamoto, Y.; Mitomo, M. *Appl. Phys. Lett.* **2004**, *84*, 5404. (b) Chen, Y.; Gong, M.; Wang, G.; Su, Q. *Appl. Phys. Lett.* **2007**, *91*, 071117. (c) Jang, H. S.; Im, W. B.; Lee, D. C.; Jeon, D. Y.; Kim, S. S. *J. Lumin.* **2007**, *126*, 371.

(3) (a) Shur, M. S.; Zukauskas, A. *Proc. IEEE* **2005**, *93*, 1691. (b) Mueller-Mach, R.; Mueller, G.; Krames, M. R.; Höppe, H. A.; Stadler, F.; Schnick, W.; Jüstel, T.; Schmidt, P. *Phys. Status Solidus A* **2005**, *202*, 1727. (c) Sato, Y.; Takahashi, N.; Sato, S. *Jpn. J. Appl. Phys., Part 2* **1996**, *35*, L838. (d) Schlotter, P.; Schmidt, R.; Schneider, J. *Appl. Phys. A.* **1997**, *64*, 417. (e) Mills, A. *Adv. Semicond. Mag.* **2005**, *18*, 32.

(4) (a) Park, J. K.; Lim, M. A.; Kim, C. H.; Park, H. D.; Park, J. T.; Choi, S. Y. *Appl. Phys. Lett.* **2003**, *82*, 683. (b) Park, J. K.; Choi, K. J.; Park, S. H.; Kim, C. H.; Kim, H. K. *J. Electrochem. Soc.* **1968**, *115*, 642. (c) Li, J.; Watanabe, T.; Wada, H.; Setoyama, T.; Yoshimura, M. *Chem. Mater.* **2007**, *19*, 3592. (d) Piao, X.; Machida, K.-I.; Horikawa, T.; Hanzawa, H.; Shimomura, Y.; Kijima, N. *Chem. Mater.* **2007**, *19*, 4592. (e) Zeuner, M.; Hintze, F.; Schnick, W. *Chem. Mater.* **2009**, *21*, 336.

10.1021/ja9092456

therefore has potential application as a blue phosphor in near-UV LEDs. The properties of Ce^{3+} in $CaBPO_5$, $LiCaPO_4$, and Li_2CaSiO_4 have also been studied using time-resolved spectroscopy at temperatures between 10 and 300 K. The band gap of the host materials, their Stokes shifts, and their luminescence decay time data have been completely determined.[5] Previously, we examined the structure, photoluminescence, thermal stability, and CIE chromaticity index of mixed orthophosphates with the formula $A^IB^{II}PO_4$, including $KSrPO_4:Eu^{2+}$, $KSrPO_4$:Ln (Ln = Eu, Tb, and Sm), $KBaPO_4$:Ln (Ln = Eu, Tb, and Sm), and $LiZn_{1-x}PO_4:Mn_x$.[5]

To the best of our knowledge, this investigation is the first to demonstrate versatile phosphate phosphors $ABPO_4$:RE (A = Li, K; B = Sr, Ba; RE = Eu^{2+}, Tb^{3+}, and Sm^{3+}) by simulation and calculation using the GSAS program and spin-polarized generalized gradient approximation plus a correction of an on-site Coulombic interaction (GGA+U) scheme, which were adopted herein to examine the structure refinements and the electronic structures of orthophosphate systems. This study determines the contrast between the orthophosphate host families and explores their chemical and physical properties. Recently, we determined the characteristics of a series of phosphate phosphors, including their crystal structure, photoluminescence, lifetime, thermal stability, particle size, the relationship between the band gap of their electronic structures, and their luminous mechanisms. We also constructed an available model to explain a possible mechanism of electron transition in the $KSrPO_4$:Eu system.

Experimental Section

Materials and Synthesis. A series of phosphate compounds were prepared in solid state reactions. Stoichiometric amounts of $(NH_4)_2HPO_4$ (Aldrich, 99.9%), Li_2CO_3 (Acros, 99%), K_2CO_3 (Aldrich, 99.99%), $SrCO_3$ (Aldrich, 99.99%), $BaCO_3$ (Aldrich, 99.99%), Eu_2O_3 (Aldrich, 99.99%), Tb_4O_7 (Aldrich, 99.99%), and Sm_2O_3 (Acros, 99.99%) were ground in an agate mortar for 30 min to mix them homogeneously. The mixtures were placed in alumina crucibles with covers and fired at 600 °C for 3 h in air atmosphere in an electric tube furnace, and the sintered products were then crushed into powder. The products were ground again in an agate mortar. The powder products were fired at 1300 °C in a reducing (N_2/H_2 = 95:5) atmosphere for 3 h. After firing, the samples were cooled to room temperature in the furnace, and ground again into powder for subsequent use.

Characterization. The composition and phase purity of the products were studied by X-ray diffraction (XRD) using a PANalytical XPert'Pert PRO diffractometer that was operated in transmission mode with Cu Kα radiation (λ = 1.5418 Å). The data were collected over a 2θ range from 20° to 90° at intervals of 0.02° with a counting time of 30 s per step. Structural refinements of X-ray diffractograms were made using the GSAS (general structure analysis system) program.[6] The photoluminescence (PL) spectra were obtained using a FluoroMax-3 and FluoroMax-P spectrophotometer at room temperature. Thermal quenching was identified using a heating apparatus (THMS-600) in combination with PL equipment. SEM micrographs of products were obtained using a field emission scanning electron microscope (FE-SEM, JSM-6700F, JEOL). The particle size distribution was measured using a laser diffraction system, CILAS1064.

Computational Method. Density functional calculations were made with the generalized gradient approximation (GGA-PBE) to investigate the electronic structures of $KSrPO_4$ and $KSrPO_4$:Eu systems. The electronic calculations are made using the full-potential projector augmented wave (PAW) method, as implemented in the VASP code[7] to compare the results with the experimental datum, the crystal structure that was determined by XRD measurement

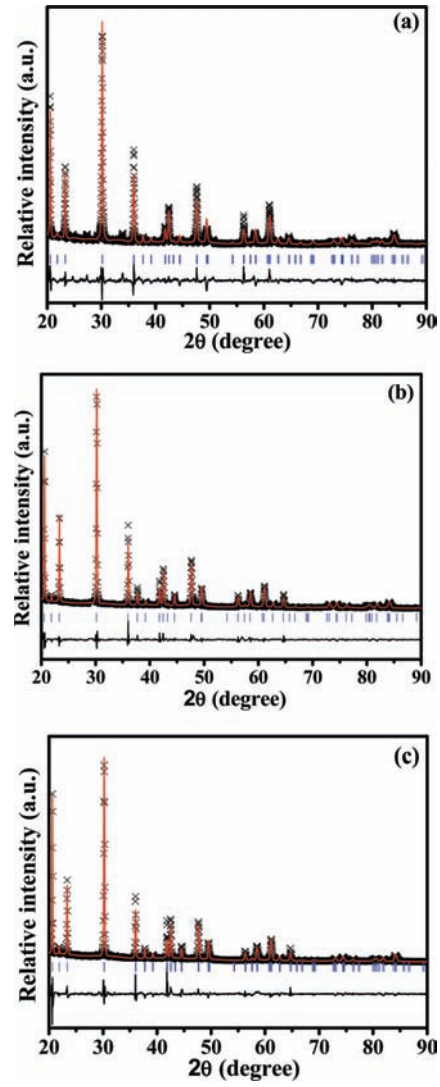

Figure 1. Experimental (crosses), calculated (solid line), and difference (bottom) results of XRD refinement of (a) $LiSr_{0.9}PO_4:Eu_{0.1}$, (b) $LiSr_{0.9}PO_4:Tb_{0.1}$, and (c) $LiSr_{0.9}PO_4:Sm_{0.1}$.

for the calculations. To simulate the 3.125% Eu-doped system, a 2 × 2 × 2 supercell, including a single Eu that replaces one Sr atom, is employed. The Brillouin zone samplings use the 4 × 5 × 3 and 2 × 2 × 2 *k*-point grids for the primitive cell and supercell, respectively. The SCF energy convergence threshold is set as 10^{-6} eV/atom to ensure the accuracy of the electronic calculation. The electronic structure of the optimized crystal geometry is obtained by conjugate-gradient calculation with a 3 × 10^{-2} eV/Å force convergence criterion. The cutoff energy for the plane wave basis is 400 eV, but our results are also tested with higher cutoff energies of up to 800 eV. In order to obtain the electronic structure and energy gaps with a higher accuracy, the on-site Coulombic interaction of Eu 4f-electrons has also been considered within the GGA+U scheme with Coulombic energy U = 2.0 eV and exchange J = 0.7 eV.[7]

Results and Discussion

XRD Refinement and Crystal Parameters. Phosphates $ABPO_4$ (A = Li, K; B = Sr, Ba) with a variety of phases crystallize into three basic structures, depending on the sizes of the cations. Their optical and ferroelectric properties were also determined in few scientific literature.[8] Herein the XRD patterns of rare-earth doped $LiSrPO_4$ are identical to those of the crystal growth

Table 1. Crystallographic Data for Versatile Phosphate Phosphors $LiSrPO_4$:RE (RE = Eu^{2+}, Tb^{3+}, and Sm^{3+})

$LiSr_{0.9}PO_4:Eu_{0.1}$		$LiSr_{0.9}PO_4:Tb_{0.1}$		$LiSr_{0.9}PO_4:Sm_{0.1}$	
Space Group					
$P6_3$ (hexagonal)		$P6_3$ (hexagonal)		$P6_3$ (hexagonal)	
Cell Parameter					
a	4.9973 (4) Å	a	4.9958 (2) Å	a	4.9974 (2) Å
b	4.9973 (4) Å	b	4.9958 (2) Å	b	4.9974 (2) Å
c	8.1571 (4) Å	c	8.1396 (3) Å	c	8.157 (3) Å
$\alpha = \beta$	90°	$\alpha = \beta$	90°	$\alpha = \beta$	90°
γ	120°	γ	120°	γ	120°
cell volume	176.41 (1) $Å^3$	cell volume	175.93 (1) $Å^3$	cell volume	176.41 (1) $Å^3$
Reliability Factors					
R_{wp}	5.92%	R_{wp}	4.75%	R_{wp}	5.92%
R_p	4.05%	R_p	3.18%	R_p	4.05%

$LiSr_{0.9}PO_4:Eu_{0.1}$

atoms	X	Y	Z	frac	U_{iso} ($Å^2$)
Li	0.333333	0.666666	0.834039	1.0000	2.50
Sr	0.000000	0.000000	−0.009519	0.943(12)	2.44
P	0.333333	0.666667	0.709393	1.0000	2.96
O(1)	0.333333	0.666666	0.866536	1.0000	2.50
O(2)	0.327637	0.363046	0.779203	1.0000	7.20
Eu	0.000000	0.000000	−0.009519	0.057(12)	2.44

$LiSr_{0.9}PO_4:Tb_{0.1}$

atoms	X	Y	Z	frac	U_{iso} ($Å^2$)
Li	0.333333	0.666666	0.680015	1.0000	2.50
Sr	0.000000	0.000000	−0.005372	0.8853	2.13
P	0.333333	0.666667	0.731673	1.0000	5.07
O(1)	0.333333	0.666666	0.662101	0.8809	2.50
O(2)	0.329382	0.370816	0.797142	0.9984	2.50
Tb	0.000000	0.000000	−0.005372	0.1147	2.13

$LiSr_{0.9}PO_4:Sm_{0.1}$

atoms	X	Y	Z	frac	U_{iso} ($Å^2$)
Li	0.333333	0.666666	0.834039	1.0000	2.50
Sr	0.000000	0.000000	−0.009519	0.8623	2.44
P	0.333333	0.666667	0.709393	1.0000	2.96
O(1)	0.333333	0.666666	0.866536	1.0000	2.50
O(2)	0.327637	0.363046	0.779203	1.0000	7.20
Sm	0.000000	0.000000	−0.009519	0.1377	2.44

$LiSrPO_4$ phase and were defined by GSAS refinement. This indicates the formation of a single phase with no impurities. Figure 1 plots experimental, calculated, and difference results from the GSAS refinement of the $LiSr_{0.9}PO_4:RE_{0.1}$ (RE = (a) Eu^{2+}, (b) Tb^{3+}, and (c) Sm^{3+}). These doped products crystallize as hexagonal structures with a space group of $P6_3$ and $a = b \neq c$, $\alpha = \beta = 90°$, $\gamma = 120°$. All of the observed peaks are consistent with the reflection conditions, lattice constants, and cell volumes in Table 1. The dopants replace Sr atoms, as expected, because the ionic radius of Sr^{2+} (1.40 Å) exceeds that of Li^+ (0.90 Å). The lattice constants and cell volumes increase with the ionic radius of dopants, according to Vegard's rule.[5,9]

Figure 2 shows the X-ray powder diffraction (XRD) patterns of the series of samples $KSr_{1-x}PO_4:RE_x$ (RE = (a) Eu^{2+}, (b) Tb^{3+}, and (c) Sm^{3+}) and $KBa_{1-x}PO_4:RE_x$ (RE = (d) Eu^{2+}, (e) Tb^{3+}, and (f) Sm^{3+}). All of the experimental XRD patterns of the samples were identified by comparison with the reference JCPDS database (33-1045, $KSrPO_4$; 33-0996, $KBaPO_4$). The comparison demonstrates that the expected compounds were successfully synthesized. This class of compounds has an orthorhombic structure with space group *Pnma* and lattice constants $a \neq b \neq c$, $\alpha = \beta = \gamma = 90°$.

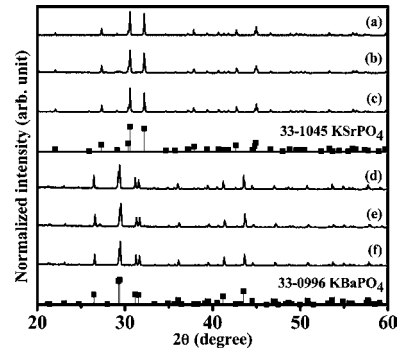

Figure 2. XRD patterns of $KSr_{1-x}PO_4:RE_x$ phosphors with (a) RE = Eu^{2+}, $x = 0.005$, (b) RE = Tb^{3+}, $x = 0.07$, (c) RE = Sm^{3+}, $x = 0.01$, and $KBa_{1-x}PO_4:RE_x$ (d) RE = Eu^{2+}, $x = 0.005$, (e) RE = Tb^{3+}, $x = 0.3$, (f) RE = Sm^{3+}, $x = 0.007$, obtained at RT using reference XRD data and the program JCPDS.

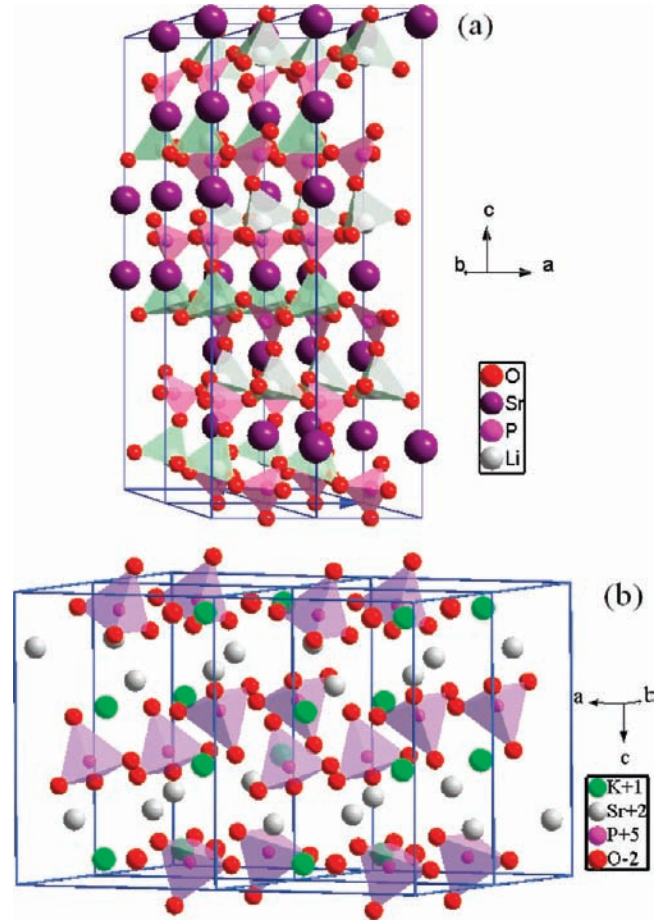

Figure 3. Schematic crystal structures of four unit cells, revealing a well-ordered array of (a) Li (gray), Sr (purple), P (pink), and O (red) atoms in a hexagonal structure; (b) K (green), Sr (gray), P (pink), and O (red) atoms in an orthorhombic structure.

Figure 3 presents the crystal structures of $LiSrPO_4$ and $KSrPO_4$; the exact atomic configurations were identified by X-ray powder diffraction and GSAS refinement. The three-dimensional framework of this novel lithium strontium phosphate comprises octahedral SrO_6, tetrahedral PO_4, and LiO_4, with large tunnels in the *a* and *b* directions. The Sr metal ion is divalent and has a slightly distorted octahedral coordination, with the oxygen atoms at the corners of octahedron. The distortion of the polyhedra is caused mainly by the adjustment stresses between the polyhedra of

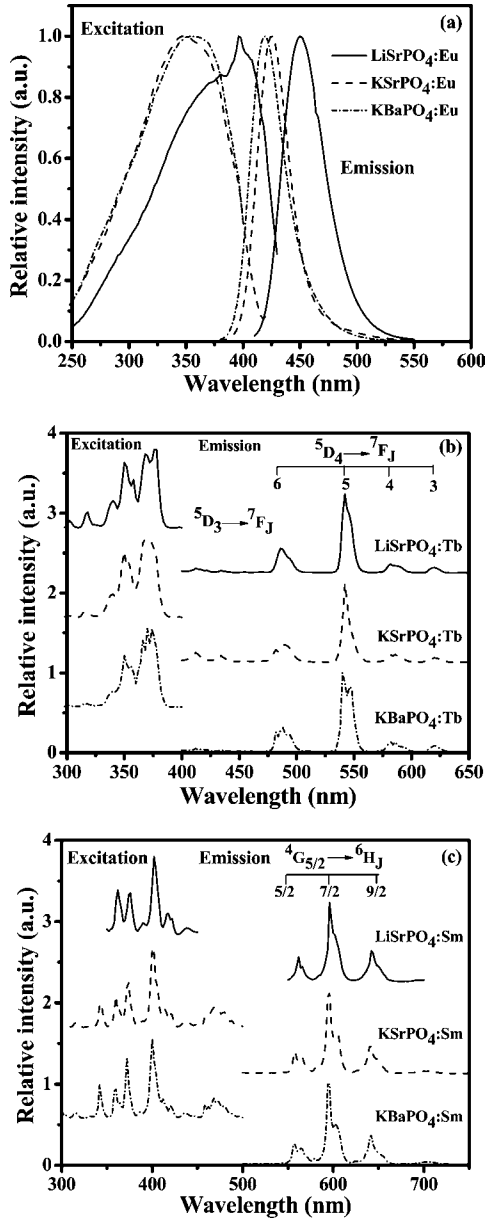

Figure 4. PLE and PL spectra of (a) $AB_{1-x}PO_4:Eu_x$ (A = Li, K; B = Sr, Ba) were obtained at RT; peak positions are given in Table 2. (b) $AB_{1-x}PO_4:Tb_x$ (A = Li, K; B = Sr, Ba), (PLE monitored at 542 nm and PL excited at 378 nm) and (c) $AB_{1-x}PO_4:Sm_x$ (A = Li, K; B = Sr, Ba), (PLE monitored at 596 nm and PL excited at 402 nm).

Table 2. Excitation and Emission Bands, Stokes Shift, and Critical Distance of RE-Doped $ABPO_4$ (A = Li, K; B = Sr, Ba; RE = Eu^{2+}, Tb^{3+}, and Sm^{3+})

$ABPO_4$	excitation band/nm (max.)	emission band/nm (max.)	Stokes shift/cm^{-1}	critical distance/Å
$LiSr_{0.930}PO_4:Eu_{0.070}$	396	445	2781	10.6
$KSr_{0.995}PO_4:Eu_{0.005}$	360	424	4193	33.5
$KBa_{0.995}PO_4:Eu_{0.005}$	360	420	3968	34.6
$LiSr_{0.950}PO_4:Tb_{0.050}$				11.9
$KSr_{0.930}PO_4:Tb_{0.070}$	378	420−450, 489, 542, 588, 621	∼8000	13.9
$KBa_{0.700}PO_4:Tb_{0.300}$				8.8
$LiSr_{0.990}PO_4:Sm_{0.010}$				20.3
$KSr_{0.990}PO_4:Sm_{0.010}$	400	562, 596, 643	∼8220	26.6
$KBa_{0.993}PO_4:Sm_{0.007}$				30.9

Table 3. CIE Chromaticity Coordinates of RE-Doped $ABPO_4$ (A = Li, K; B = Sr, Ba; RE = Eu^{2+}, Tb^{3+}, and Sm^{3+})

$LiSr_{1-x}PO_4:Eu_x$			$LiSr_{1-x}PO_4:Tb_x$			$LiSr_{1-x}PO_4:Sm_x$		
	CIE chromaticity			CIE chromaticity			CIE chromaticity	
Eu con. (x)	x	y	Tb con. (x)	x	y	Sm con. (x)	x	y
0.01	0.1499	0.0374	0.03	0.2793	0.4672	0.005	0.5784	0.4208
0.03	0.1504	0.038	0.05	0.289	0.5307	0.007	0.5794	0.4198
0.05	0.1475	0.0414	0.10	0.297	0.5326	0.010	0.5788	0.4203
0.07	0.1446	0.0515	0.15	0.2986	0.5055	0.030	0.5797	0.4195
0.10	0.14	0.0679				0.050	0.5772	0.4219

$KSr_{1-x}PO_4:Eu_x$			$KSr_{1-x}PO_4:Tb_x$			$KSr_{1-x}PO_4:Sm_x$		
	CIE chromaticity			CIE chromaticity			CIE chromaticity	
Eu con. (x)	x	y	Tb con. (x)	x	y	Sm con. (x)	x	y
0.001	0.1617	0.0222	0.01	0.2957	0.4605	0.003	0.5631	0.4312
0.003	0.1617	0.0220	0.03	0.2994	0.5398	0.005	0.5691	0.4264
0.005	0.1610	0.0238	0.05	0.2954	0.5373	0.010	0.5723	0.4237
0.007	0.1611	0.0236	0.07	0.2999	0.5473	0.050	0.5628	0.4313
0.010	0.1620	0.0210	0.10	0.3059	0.5286	0.100	0.5562	0.4365

$KBa_{1-x}PO_4:Eu_x$			$KBa_{1-x}PO_4:Tb_x$			$KBa_{1-x}PO_4:Sm_x$		
	CIE Chromaticity			CIE Chromaticity			CIE Chromaticity	
Eu con. (x)	x	y	Tb con. (x)	x	y	Sm con. (x)	x	y
0.001	0.1623	0.0193	0.05	0.2807	0.4900	0.005	0.5668	0.4286
0.003	0.1605	0.0213	0.10	0.2868	0.5188	0.007	0.5691	0.4268
0.005	0.1610	0.0207	0.20	0.2902	0.5400	0.010	0.5701	0.4260
0.007	0.1600	0.0218	0.30	0.2916	0.5542	0.030	0.5694	0.4265
0.010	0.1592	0.0238	0.40	0.2919	0.5450	0.050	0.5651	0.4300

different dimensions that share edges. The structure of $LiSrPO_4$, shown in Figure 3a can alternatively be viewed as containing octahedral SrO_6, tetrahedral PO_4, or LiO_4 that is connected by an oxygen bridge which cross-links the Sr and Li atoms, to generate a three-dimensional composite framework structure. The crystal structures of $KBPO_4$ (B = Sr, Ba) were not analyzed using GSAS refinement, because the compounds have already been reported to have the same β-K_2SO_4 structure with space group *Pnma*. Rather, the series of orthophosphate structures are compared with $LiSrPO_4$. Figure 3b depicts the structure that is formed by regular PO_4^{3-} tetrahedra that surround the K^+ and Sr^{2+} cations in 10-fold and 9-fold coordination, respectively. The framework is constructed from successive arrays of K atoms and tetrahedral PO_4 of the same

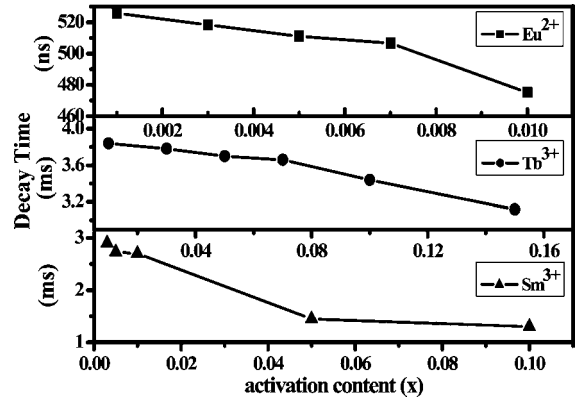

Figure 5. Decay time vs activation concentration of $KSrPO_4$ with different dopants: (a) Eu^{2+}, (b) Tb^{3+}, and (c) Sm^{3+}. Decay curves are given in Supporting Information S3.

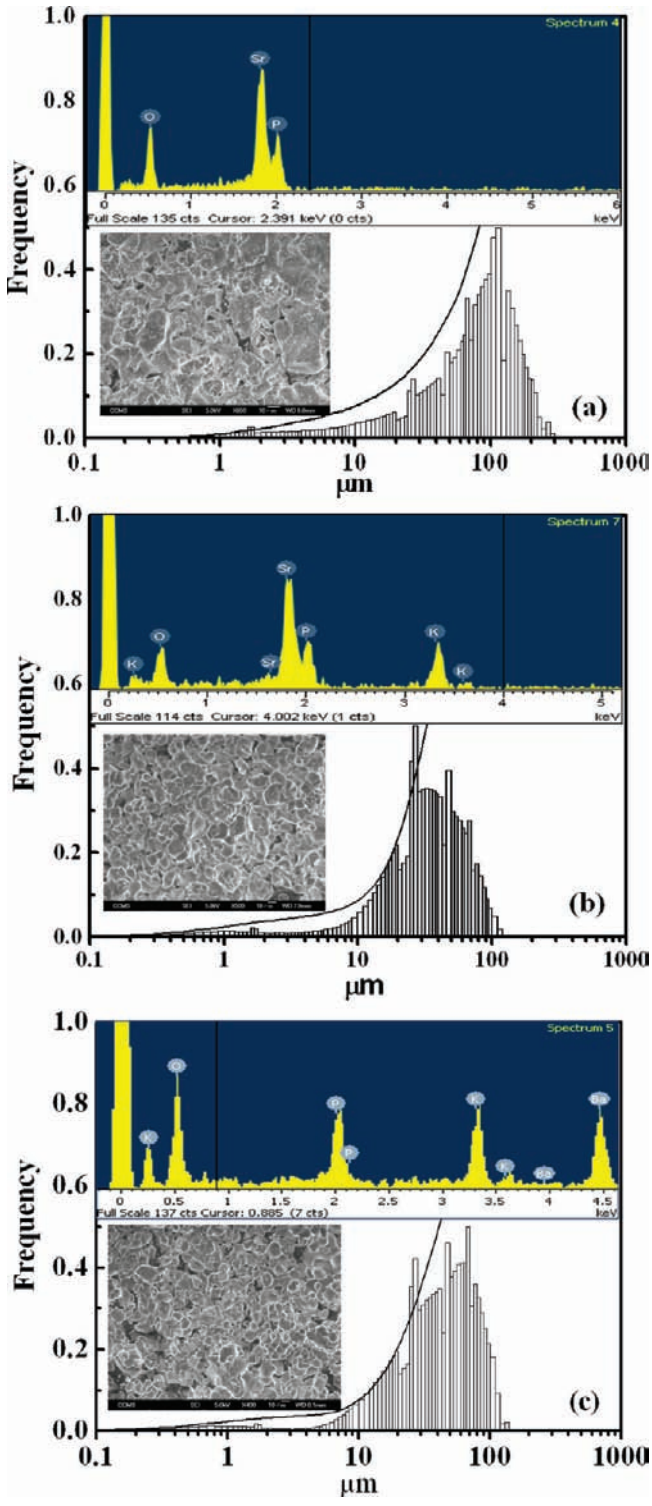

Figure 6. Particle size distribution, SEM image, and EDX data for pure hosts: (a) $LiSrPO_4$, (b) $KSrPO_4$, and (c) $KBaPO_4$.

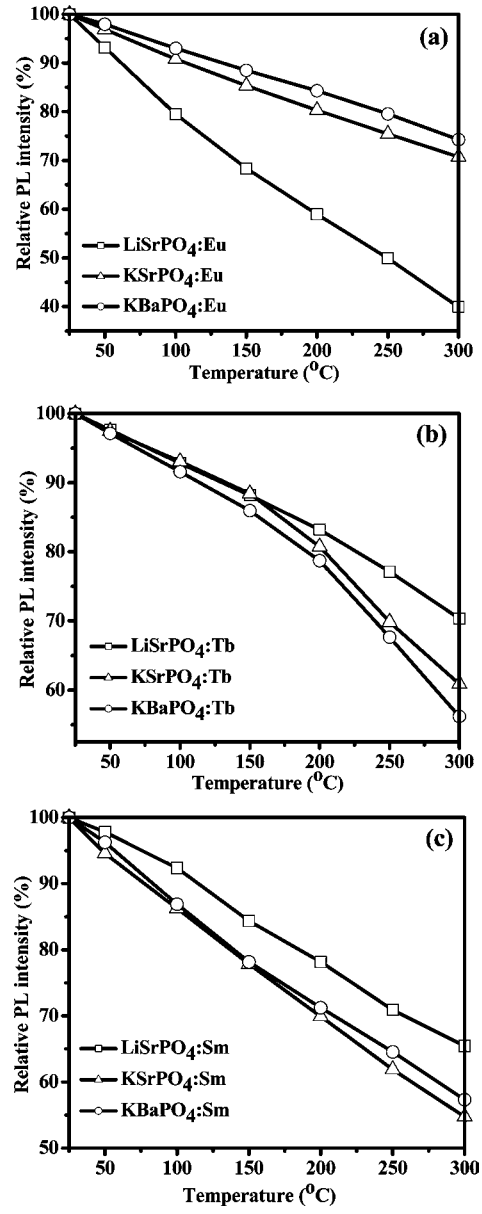

Figure 7. Temperature-dependence of emission peak intensity of (a) $AB_{1-x}PO_4:Eu_x$ (A = Li, K; B = Sr, Ba), and peak positions described in Table 2. (b) $AB_{1-x}PO_4:Tb_x$ (A = Li, K; B = Sr, Ba), (PLE monitored at 542 nm and PL excited at 378 nm) and (c) $AB_{1-x}PO_4:Sm_x$ (A = Li, K; B = Sr, Ba), (PLE monitored at 596 nm and PL excited at 402 nm).

height. The barium and potassium atoms are surrounded very compactly by tetrahedral PO_4.[9,10]

Analysis of Photoluminescence Properties. The emission color of Eu^{2+} is strongly dependent on the crystal lattices. Eu^{2+}-doped orthophosphate phosphors usually emit blue luminescence with a broadband under ultraviolet excitation at 360 nm. Figure 4a displays excitation and emission spectra of Eu^{2+}-doped $ABPO_4$ (A = Li, K; B = Sr, Ba). The excitation spectra of these compounds are obtained in the range 300−400 nm. The emission spectra reveal broadband from the 5d→4f transition of europium, as shown in the right-hand side of Figure 4a. Table 2 clearly demonstrates that the $LiSrPO_4$:Eu shows significant redshifts in excitation and emission bands, which is largely different from $KSrPO_4$:Eu and $KBaPO_4$:Eu. The phenomenon indicates that the large crystal-field splitting and nephelauxetic effect observed in $LiSrPO_4$:Eu by considering the local structure of Eu^{2+}. However, the excitation and emission wavelengths of the series of $KB_{1-x}PO_4:Eu_x$ (B = Sr, Ba) are very similar, because the crystal structures are similar.[11] The series of sharp excitation peaks are assigned to the $^5D_3 \rightarrow {}^7F_J$ (J = 2, 3, 4, 5, 6) transition, and the lower emission-state $^5D_4 \rightarrow {}^7F_J$ (J = 3, 4, 5, 6) transition between 450 and 650 nm corresponds to the typical 4f→4f intraconfiguration forbidden transitions of Tb^{3+}. Figure 4b presents the excitation and emission spectra of $AB_{1-x}PO_4:Tb_x$ (A = Li, K; B = Sr, Ba). A broad excitation band with a maximum wavelength at 378 nm indicates that near-UV LEDs

can excite all terbium-doped phosphors. The phosphors emit yellowish green light, approximating green luminescence with a peak wavelength of 542 nm. The broad excitation spectrum is associated with f−f transitions. The major emission peak that is centered at 542 nm corresponds to the $^5D_4-^7F_5$ transition, while those at 489, 588, and 621 nm correspond to the$^5D_4-^7F_6$, $^5D_4-^7F_4$, and $^5D_4-^7F_3$ transitions, respectively. These emissions are similar to those observed in $Y_3Al_5O_{12}$:Tb^{3+} and $SrIn_2O_4$:Tb^{3+} phosphors.[12] For all $AB_{1-x}PO_4$:Tb_x (A = Li, K; B = Sr, Ba) phosphors, a less intense blue emission in the range 420−450 nm was observed; it is caused by the relaxation of the $^5D_3$ level. Usually, the nonradiative cross-relaxation mechanism favors a greater occupancy of $^5D_4$ level at the expense of the $^5D_3$ level: $Tb^{3+}(^5D_3) + Tb^{3+}(^7F_6) \rightarrow Tb^{3+}(^5D_4) + Tb^{3+}(^7F_0)$. This effect is responsible for the enhancement in the green emissions by transitions from the highly populated $^5D_4$ level.[12] These rugged excitation bands are observed mainly at 400 nm because of intraconfigurational 4f transitions from trivalent samarium ion. The emission spectra of all $AB_{1-x}PO_4$:Sm_x include the characteristic red luminescence of Sm^{3+}, which consists of the sharp strong peak at 596 nm and the weak peaks at 562 and 643 nm (Figure 4c), consistent with $^4G_{5/2} \rightarrow {}^6H_J$ (J = 5/2, 7/2, 9/2). The Sm^{3+} ions have the $4f^5$ configuration and are therefore labeled as Kramer ions because of their electronic states that are at least doubly degenerated for any crystal field perturbation in the vacuum ultraviolet and the near-ultraviolet range. This effect can be exploited converting to white light for LED application.[13]

Table 2 presents the Stokes shift, excitation, emission position, and critical distance of the versatile phosphate phosphors $ABPO_4$:RE (A = Li, K; B = Sr, Ba; RE = Eu^{2+}, Tb^{3+}, Sm^{3+}). Figure SI 1−3 in Supporting Information (S1) includes the emission intensity as a function of the activator concentration for different phosphate host matrixes. According to Dexter and Schulman, concentration quenching is frequently caused by energy transfer from one activator to another, until an energy sink in the lattice is reached. The average distance between activators can be expressed using the relation that was proposed by Blasse and Grabmaier:[14]

$$R_c \approx 2\left(\frac{3V}{4\pi x_c N}\right)^{1/3} \quad (1)$$

where x denotes the total concentration of dopants; N is the number of available sites for the dopant in the unit cell, and V is the volume of the unit cell. For an $LiSrPO_4$ host, N is 4 for Eu^{2+}, Tb^{3+}, and Sm^{3+} dopants, and the V obtained from the XRD refinement results, is 176 Å^3, based on the assumption that the lattice parameters remain almost constant as Eu^{2+}, Tb^{3+}, and Sm^{3+} doping levels vary. Accordingly, the distances are calculated to be 10.6, 11.89, and 20.33 Å by taking x as the Eu^{2+}, Tb^{3+}, and Sm^{3+} concentrations, 0.070, 0.050, and 0.010, respectively. The critical distance of the doped $KB_{1-x}PO_4$ (B = Sr, Ba) is also presented in Table 2. Figure SI 4−6 in Supporting Information (S2) presents the CIE chromaticity diagrams of the samples. The entire chromaticity index (x, y) for various elements (A = Li, K; B = Sr, Ba) and activators (RE = Eu^{2+}, Tb^{3+}, Sm^{3+}) were calculated, as shown in Table 3.

Based on the above-mentioned PL spectra of a series of samples, $KSr_{1-x}PO_4$:RE_x, the relationship between concentration quenching behavior and lifetime is considered. Supporting Information (S3) includes decay curves for $KSr_{1-x}PO_4$:RE_x (RE = Eu^{2+}, Tb^{3+}, Sm^{3+}) with various activation concentrations are depicted in. The lifetimes (τ) were estimated to be 530−470 ns for Eu^{2+}, 4−3 ms for Tb^{3+}, and 3−1 ms for Sm^{3+} by single-exponential as plotted in Figure SI 7−9 (Supporting Information (S1)). Consequently, Figure 5 plots the decay time vs activation concentration of $KSrPO_4$ with different dopants (a) Eu^{2+}, (b) Tb^{3+}, and (c) Sm^{3+}. Interestingly, the decay time begins to decrease abruptly at a certain doped function, which was defined as the critical concentration according to quenching behavior. Actually, the nonradiative and self-absorption rate of the internal doped ions evidently increase when activators cross the critical separation between donor (activator ion) and acceptor (quenching site). These curves are associated with concentration quenching of the photoluminescence spectra that are proposed in Supporting Information (S1).[14]

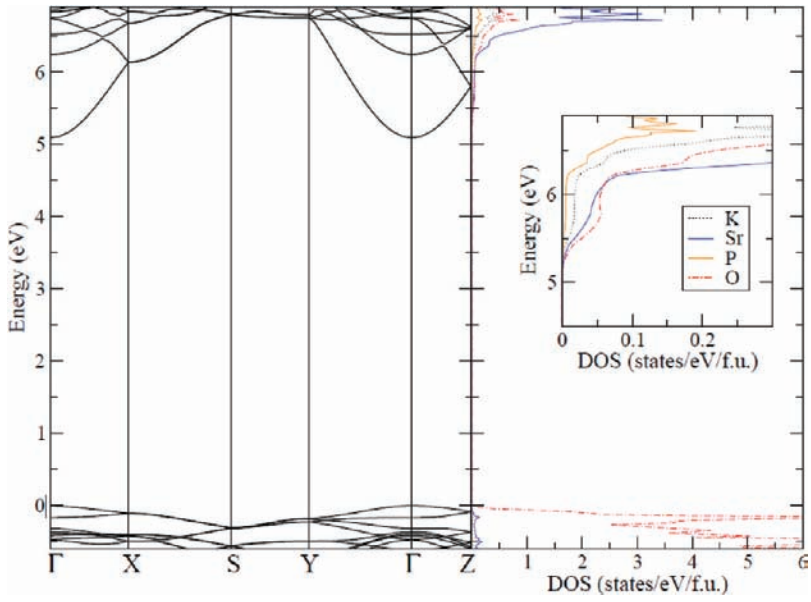

Figure 8. Band structures and DOS of pure $KSrPO_4$. The energy reference (0 eV) is set to the energy of the most energetic occupying electron, which is also the top of the VB.

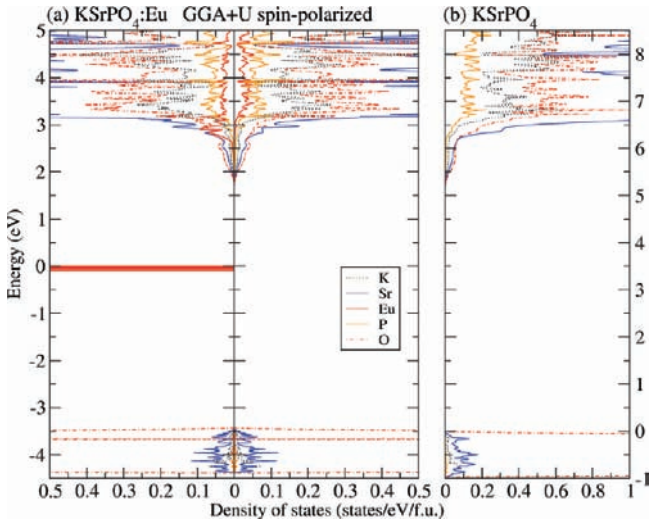

Figure 9. DOS of $KSrPO_4$ (a) with 3.125% Eu doping given by GGA+U and (b) without doping. Energy references (0 eV) are set as the top of the electron occupation. The DOS spectra for majority and minority spins of $KSrPO_4$:Eu in (a) are displayed in the left and right panels, respectively.

Morphology. The morphologies and constituent elements of the samples were investigated by the SEM, EDX, and observations of particle size distribution. Figure 6 depicts the particle size, an electron microscope image, and EDX data for all pure phosphate hosts at room temperature. The mostly like scurf crystals of $LiSrPO_4$ with coated surfaces that grow together to a diameter of around 100 μm and form the aggregates that are displayed in Figure 6a, and are separated again by ball-milling to form packages for LEDs. Parts b and c of Figure 6 demonstrate that $KB_{1-x}PO_4$ (B = Sr, Ba) has a smoother surface than $LiSrPO_4$ and an average diameter of 30−50 μm. EDX was employed to characterize the composition of the pure host that was annealed at 1300 °C, as presented at the top of Figure 6. It confirms that the formation of all samples by the synthesis method herein according to the presence of K, Sr, Ba, P, and O. However, the light Li element was hard to identify by SEM-EDX measurement.

Thermal Quenching. The thermal quenching of phosphors used in white LEDs must be understood. The temperature-dependent luminescent properties were measured between 25 and 300 °C and the results plotted in Figure 7. The emission intensity declined as the temperature increased, because of thermal quenching which is presented in the configurationally coordinate diagram.[15] The luminescent intensity of activators at various temperatures has never been elucidated with reference to crystal structure and the coordination environment. Figure 7a plots the decreasing rate of luminescent intensity from $LiSrPO_4:Eu^{2+}$, to $KSrPO_4:Eu^{2+}$, to $KBaPO_4:Eu^{2+}$ as temperature increases. $LiSrPO_4:Eu^{2+}$ has worse thermal stability than $KSrPO_4:Eu^{2+}$ because Li^+ promotes the conversion of Eu^{2+} to Eu^{3+} more than does K^+ ion, based on electronic affinity. Second, Eu^{2+} substitutes at the Sr^{2+} sites are distinct from crystal structures (hexagonal or orthorhombic). Third, the only small difference between $KSrPO_4:Eu^{2+}$ and $KBaPO_4:Eu^{2+}$ is the similar alkaline-earth metals. $KBaPO_4:Eu^{2+}$ is more thermally stable than $KSrPO_4:Eu^{2+}$, because of the thermally active phonon-assisted excitation from heavy ions to light ions. The thermal quenching temperature, T_{50}, is defined as the temperature at which the emission intensity is 50% of its original value. The samples of $KBPO_4:Eu^{2+}$ (B = Sr, Ba) have a higher T_{50}, exceeding 300 °C, than $LiSrPO_4:Eu^{2+}$ which has a T_{50} of 250 °C, indicating its greater thermal stability as a luminescent material for white LEDs.

Tb^{3+} forms a competitive hole-trapping center, as has been confirmed by the detection of lattice defect levels.[16] This work can explain the thermal conditions of Tb^{3+} in Figure 7b. If the neutral composition is formed by the replacement of the divalent cation (B site) by trivalent cation (Tb^{3+}) and an electron, then $LiSrPO_4:Tb^{3+}$ must have the best thermal stability because the Li^+ ion captures more electrons than the K^+ ion. Alternatively, $KBaPO_4:Tb^{3+}$ has poor thermal stability because the Ba^{2+} ion traps more holes than the Sr^{2+} ion. The intensity of $KBaPO_4:Tb^{3+}$ decreased rapidly following the conversion of Tb^{3+} to Tb^{4+}. All of the $ABPO_4:Tb^{3+}$ have a high T_{50} of over 300 °C. Interestingly, the more thermally stable $LiSrPO_4:Sm^{3+}$ retains Sm^{3+} without unnecessary electrons, which is shown in Figure 7c. The phenomenon is related to the crystal structure and the coordination environment of the activators at different temperatures. Finally, the above findings are captured in the following eq 2.[16]

$$\begin{aligned} Eu^{2+} &\rightarrow Eu^{3+} + e^- \\ Tb^{3+} + h^+ &\rightarrow Tb^{4+} \\ Sm^{3+} + e^- &\rightarrow Sm^{2+} \end{aligned} \qquad (2)$$

Band Structure and Mechanism of Electron Transition. This section explains the band structure of, and possible mechanism of electron transition in, the $KSrPO_4$:Eu system. Figure 8 presents the band structure and density of states (DOS) of pure $KSrPO_4$. The results reveal that pure $KSrPO_4$ is a direct band gap of approximately 5.09 eV at point Γ. The band gap shifts slightly to 5.11 eV if the 800 eV cutoff energy is considered. In order to estimate the electronic structures after geometrical optimization, the band gap is still about 5.12 eV, suggesting that geometrical optimization and higher energy cutoff has only a weak effect on the electronic structure of $KSrPO_4$ systems. According to the DOS spectra in Figure 8, the top of valence band (VB) close to 0 eV is dominated by O 2p orbitals, with only a small Sr contribution. Remarkably, both oxygen and strontium provide most of the conduction band (CB) edge near 5.12 eV. Hybridization between O 3s and Sr 5s orbitals on CB is formed through O−Sr bonding. Figure 9 depicts the electronic structure of $KSrPO_4$ before and after dilute Eu doping. When a Eu atom replaces one of the Sr atoms, the Eu 4f majority spin states are fully occupied, and the main peak of the Eu 5d states appears at about 3.0 eV above the Fermi level in Figure 9a. Interestingly, the exchange interaction acting on the Eu 4f causes a large exchange splitting of about 4.5 eV as shown in Figure SI 12 of Supporting Information (S4). Since CB starts from 1.8 eV, there is little Eu 4f contribution near the CB minimum. Unlike the localized Eu 4f orbitals illustrated in Figure 10, the Eu 5d orbitals, which hybridize with Sr 5s and O 3s states, as indicated in Figure 9, are rather dispersive. It is clear that the distribution of Eu 5d DOS expands in whole CB shown in Figure SI 13 of Supporting Information (S4). Remarkably, the separation of 3.0 eV of Eu 4f−5d main peaks corresponding to the wavelength of 414 nm, is very close to the measured emission wavelength of 424 nm. Therefore, our calculation results suggest a possible mechanism of excitation from Eu 4f to CB via Eu 5d and then main emission from the Eu 5d to Eu 4f. Based on the above discussion and Supporting Information (S4), Figure 11 presents a proposed mechanism of electron transition in the $KSrPO_4$:Eu system. Initially, the Eu 4f→CB excitation pumps electrons to delocalized CB via Eu 5d. Then the nonradiative relaxation brings the electron to the main peak

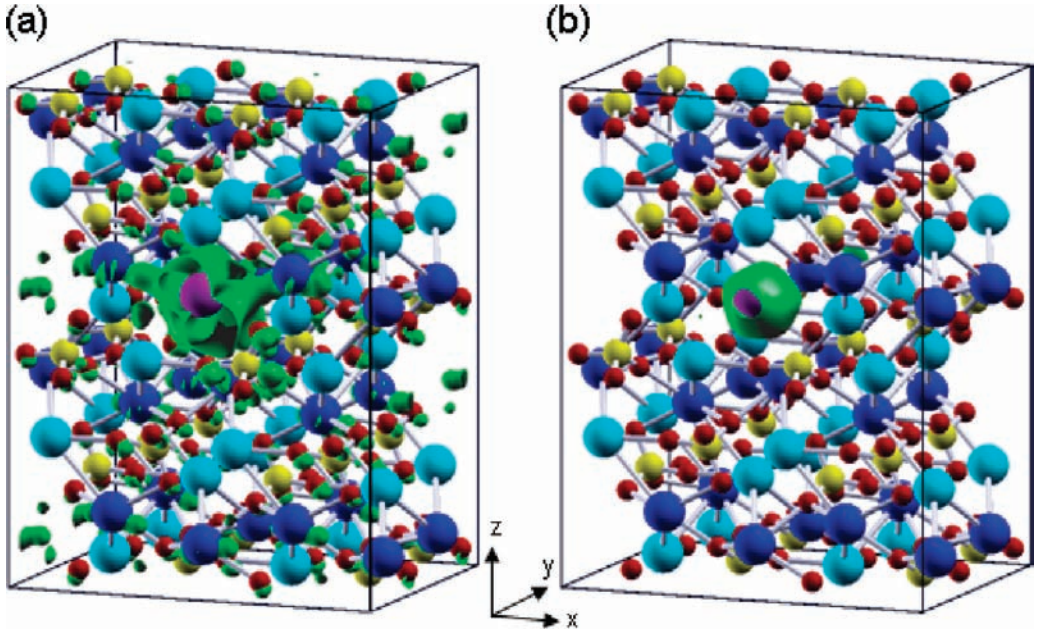

Figure 10. The majority spin orbital structures of $KSrPO_4$:Eu in energy ranges (a) 3.2−2.8 eV and (b) 0.0−0.4 eV in Supporting Information (S4), Figure SI 12d corresponding to spin-polarized GGA+U Sr 5s−O 3s−Eu 5d and Eu 4f majority spin states, respectively. Eu atom and orbital distributions are represented as purple spheres and green isosurfaces, respectively.

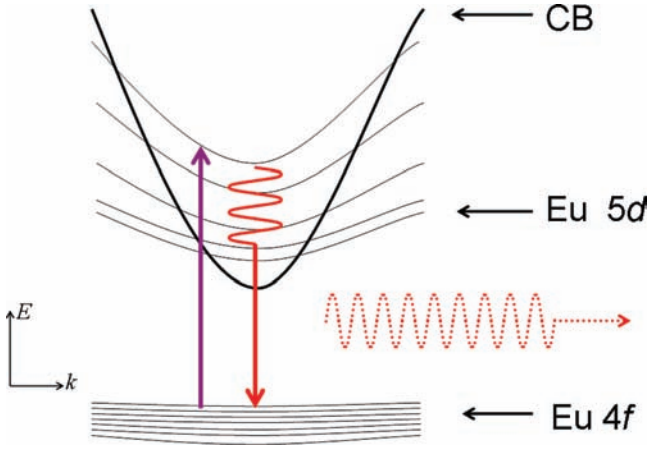

Figure 11. Possible mechanism of electronic transition in $KSrPO_4$:Eu system. Purple and red arrows represent electron transitions Eu 4f→CB via Eu 5d and Eu 5d→Eu 4f, respectively. Orange dotted arrow represents photoemission.

of Eu 5d near the lower band edge of CB. Finally, photoemission may occur in on-site Eu 5d−4f transition.

Conclusion

In summary, a simple solid-state route was adopted to fabricate a series of phosphate phosphors $ABPO_4$:RE with various compositions and activators, with A = Li, K; B = Sr, Ba; and RE = Eu^{2+}, Tb^{3+}, Sm^{3+}. Their optical properties, CIE index, Stokes shift, and critical distance were discussed. This study demonstrates that the flexibility of the produced lattice enables the photoluminescence to be tailored to satisfy specific device requirements. Three series of phosphate phosphors $ABPO_4$:RE (A = Li, K; B = Sr, Ba; RE = Eu^{2+}, Tb^{3+}, Sm^{3+}), $KBaPO_4$:Eu, $LiSrPO_4$:Tb, and $LiSrPO_4$:Sm, exhibited the most thermally stable blue, green, and red emissions, respectively. The crystal structure and the coordination environment of activators at different temperatures are responsible for the thermal stability. This work is the first to describe such a thermal quenching cascade in phosphate compounds. Although the

(5) (a) Liang, C. S.; Eckert, H.; Gier, T. E.; Stucky, G. D. *Chem. Mater.* 1993*5*, 597. (b) Wu, Z. C.; Shi, J. X.; Wang, J.; Gong, M. L.; Su, Q. *J. Solid State Chem.* **2006**, *179*, 2356. (c) Dorenbos, P.; Pierron, L.; Dinca, L.; Eijk, C. W. E. V.; Harari, A. K.; Viana, B. *J. Phys.: Condens. Matter* **2003**, *15*, 511. (d) Tang, Y. S.; Hu, S. F.; Lin, C. C.; Bagkar, N. C.; Liu, R. S. *Appl. Phys. Lett.* **2007**, *90*, 151108. (e) Lin, C. C.; Liu, R. S.; Tang, Y. S.; Hu, S. F. *J. Electrochem. Soc.* **2008**, *155*, J248. (f) Chan, T. S.; Liu, R. S.; Baginskiy, I. *Chem. Mater.* **2008**, *20*, 1215.

(6) Larson, C. Von Dreele, R. B. *Generalized Structure Analysis System (GSAS), Los Alamos National Laboratory Report LAUR 86-748*, Los Alamos National Laboratory: Los Alamos, NM, 1994.

(7) (a) Blöchl, P. E. *Phys. Rev. B* **1994**, *50*, 17953. (b) Kresse, G.; Hafner, J. *Phys. Rev. B* **1993**, *48*, 13115. (c) Kresse, G.; Furthmüller, J. *Comp. Mater. Sci* **1996**, *6*, 15. (d) Anisimov, V. I.; Solovyev, I. V.; Korotin, M. A.; Czyzyk, M. T.; Sawatzky, G. A. *Phys. Rev. B* **1993**, *48*, 16929.

(8) (a) Wanmaker, W. L.; Spier, H. L. *J. Electrochem. Soc.* **1962**, *109*, 109. (b) Blum, D.; Penzin, J. C.; Henrym, J. Y. *Ferroelectrics* **1984**, *61*, 265. (c) Engel, G. *Neues Jahrb. Mineral. Abh.* **1976**, *127*, 197. (d) Philip, L.; Marian, C. P.; Peter, G. B.; Isaac, A. *J. Mater. Chem.* **1991**, *1*, 1061.

(9) (a) Wu, Z. C.; Shi, J. X.; Wang, J.; Gong, M. L.; Su, Q. *J. Solid State Chem.* **2006**, *179*, 2356. (b) Ganguly, P.; Shah, N.; Phadke, M.; Ramaswamy, V.; Mulla, I. S. *Phys. Rev. B* **1993**, *47*, 991.

(10) (a) Ammari, L. E.; Koumiri, M. E.; Depmeier, W.; Hesse, K.-F.; Elouadi, B. *Eur. J. Solid State Inorg. Chem.* **1997**, *34*, 563. (b) Elouadi, B.; Ammari, L. E. *Ferroelectrics* **1990**, *107*, 253. (c) Masse, R.; Durif, A. *J. Solid State Chem.* **1987**, *71*, 574.

(11) (a) Li, Y. Q.; Delsing, A. C. A.; De With, G.; Hintzen, H. T. *Chem. Mater.* **2005**, *17*, 3242. (b) Xie, R. J.; Hirosaki, N.; Mitomo, M.; Yamamoto, Y.; Suehiro, T.; Sakuma, K. *J. Phys. Chem. B.* **2004**, *108*, 12027. (c) Li, Y. Q.; Van Steen, J. E. J.; Van Krevel, J. W. H.; Botty, G.; Delsing, A. C. A.; DiSalvo, F. J.; De With, G.; Hintzen, H. T. *J. Alloys Compd.* **2006**, *417*, 273.

(12) (a) Choe, J. Y.; Ravichandran, D.; Blomquist, S. M.; Kirchner, K. W.; Forsythe, E. W.; Morton, D. C. *J. Lumin.* **2001**, *93*, 119. (b) Forster, T. *Z. Naturforsch, A: Phys. Sci.* **1994**, *4*, 321. (c) Blasse, G. *Rev. Inorg. Chem.* **1983**, *5*, 319.

(13) (a) May, P. S.; Metcalf, D. H.; Richardson, F. S.; Carter, R. C.; Miller, C. E. *J. Lumin.* **1992**, *51*, 249. (b) Tang, T. P.; Lee, C. M.; Ten, F. C. *Ceram. Int.* **2006**, *32*, 665. (c) Gruber, J. B.; Bahram, Z.; Reid, M. F. *Phys. Rev.* **1999**, *60*, 15643.

(14) (a) Blasse, G. *Philips Res. Rep.* **1969**, *24*, 131. (b) Sohn, K. S.; Choi, Y. Y.; Park, H. D. *J. Electrochem. Soc.* **2000**, *147*, 1988. (c) Sohn, K. S.; Choi, Y. Y.; Park, H. D.; Choi, Y. G. *J. Electrochem. Soc.* **2000**, *147*, 2375. (d) Sohn, K. S.; Choi, Y. G.; Choi, Y. Y.; Park, H. D. *J. Electrochem. Soc.* **2000**, *147*, 3552.

mechanism of luminescence in the $KSrPO_4$:Eu system is not yet understood in detail, we recently elucidated the band structure of, and possible mechanism of electron transition in, the $KSrPO_4$:Eu system by theoretical calculation. Finally, a concise model was proposed to explain the luminescence mechanism evidently.

(15) (a) Shionoya, S., Yen, W. M., Eds. *Phosphor Handbook*; Laser & Optical Science & Technology Series; CRC Press (Taylor and Francis): Boca Raton, FL; New York, 1998; pp 65−220. (b) Kim, J. S.; Park, Y. H.; Kim, S. H.; Choi, J. C.; Park, H. L. *Solid State Commun.* **2005**, *133*, 445. (c) Xie, R.-J.; Hirosaki, N.; Kimura, N.; Sakuma, K.; Mitomo, M. *Appl. Phys. Lett.* **2007**, *90*, 191101.

(16) (a) Yamamoto, H.; Urabe, K. *J. Electrochem. Soc.* **1982**, *129*, 2069. (b) Struck, C. W.; Fonger, W. H. *Phys. Rev. B* **1971**, *4*, 22. (c) Robbins, D. J.; Cockayne, B.; Glasper, J. L.; Lent, B. *J. Electrochem. Soc.* **1979**, *126*, 1221. (d) Yamamoto, H.; Kano, T. *J. Electrochem. Soc.* **1979**, *126*, 305.

Acknowledgment. We thank the National Science Council of the Republic of China, Taiwan (Contract Nos. NSC 97-2113-M-002-012-MY3 and NSC 97-3114-M-002-005), the Ministry of Economic Affairs of the Republic of China, Taiwan (Contract No. MOEA-97-EC-17-A-07-S1-043) and Epistar Corporation (Hsinchu, Taiwan) for financially supporting this research.

Supporting Information Available: Photoluminescence (PL) measurements, CIE chromaticity coordinates, lifetime measurements, and electronic structure calculations of the $A^IB^{II}PO_4$ (A^I = monovalent cation, B^{II} = divalent cation) samples were shown in S1, S2, S3, and S4, respectively. This material is available free of charge via the Internet at http://pubs.acs.org.

JA9092456